October 28, 2016

An assessment of the radiative effects of ice supersaturation based on in situ observations

Xiaoxiao Tan, *Peking University*
Yi Huang, *McGill University*
Minghui Diao, *San Jose State University*
Aaron Bansemer, *National Center for Atmospheric Research*
Mark A. Zondlo, *Princeton University*, et al.

AGU PUBLICATIONS

Geophysical Research Letters

RESEARCH LETTER
10.1002/2016GL071144

An assessment of the radiative effects of ice supersaturation based on in situ observations

Xiaoxiao Tan[1,2], Yi Huang[2], Minghui Diao[3], Aaron Bansemer[4], Mark A. Zondlo[5], Joshua P. DiGangi[6], Rainer Volkamer[7], and Yongyun Hu[1]

[1]Department of Atmospheric and Oceanic Sciences, Peking University, Peking, China, [2]Department of Atmospheric and Oceanic Sciences, McGill University, Montreal, Quebec, Canada, [3]Department of Meteorology and Climate Science, San Jose State University, San Jose, California, USA, [4]Mesoscale and Microscale Meteorology Laboratory, National Center for Atmospheric Research, Boulder, Colorado, USA, [5]Department of Civil and Environmental Engineering, Princeton University, Princeton, New Jersey, USA, [6]Chemistry and Dynamics Branch, NASA Langley Research Center, Hampton, Virginia, USA, [7]Department of Chemistry and Biochemistry and CIRES, University of Colorado Boulder, Boulder, Colorado, USA

Key Points:
- Ice supersaturation (ISS) impacts on radiative flux and heating rates are quantified
- Mistaking ISS excess water vapor as cirrus clouds would induce significant radiative errors
- ISS radiative impact is dependent on pre-existing cloud ice

Supporting Information:
- Supporting Information S1

Correspondence to:
Y. Huang,
yi.huang@mcgill.ca

Citation:
Tan, X., Y. Huang, M. Diao, A. Bansemer, M. A. Zondlo, J. P. DiGangi, R. Volkamer, and Y. Hu (2016), An assessment of the radiative effects of ice supersaturation based on in situ observations, *Geophys. Res. Lett.*, *43*, 11,039–11,047, doi:10.1002/2016GL071144.

Received 15 SEP 2016
Accepted 12 OCT 2016
Accepted article online 13 OCT 2016
Published online 28 OCT 2016

Abstract We use aircraft observations combined with the reanalysis data to investigate the radiative effects of ice supersaturation (ISS). Our results show that although the excess water vapor over ice saturation itself has relatively small radiative effects, mistaking it as ice crystals in climate models would lead to considerable impacts: on average, +2.49 W/m^2 change in the top of the atmosphere (TOA) radiation, −2.7 W/m^2 change in surface radiation, and 1.47 K/d change in heating rates. The radiative effects of ISS generally increase with the magnitudes of supersaturation. However, there is a strong dependence on the preexisting ice water path, which can even change the sign of the TOA radiative effect. It is therefore important to consider coexistence between ISS and ice clouds and to validate their relationship in the parameterizations of ISS in climate models.

1. Introduction

Ice supersaturation (ISS) is a condition where relative humidity with respect to ice (RHi) is greater than 100%, and it frequently occurs in the upper troposphere and lower stratosphere (UTLS) [e.g., *Heymsfield et al.*, 1998; *Gierens et al.*, 1999; *Gettelman et al.*, 2006; *Jensen et al.*, 2013; *Diao et al.*, 2014]. As the prerequisite condition for ice crystal formation, ISS can exist in both clear-sky and in-cloud conditions, as previously reported by in situ and satellite observations [e.g., *Brewer*, 1946; *Heymsfield et al.*, 1998; *Comstock et al.*, 2004; *Gettelman et al.*, 2006; *Krämer et al.*, 2008; *Lamquin et al.*, 2012; *Diao et al.*, 2013]. In fact, aircraft observation analysis showed that a large percentage (>50%) of in-cloud conditions are ice supersaturated, and the in-cloud RHi magnitudes can be over 150% for temperatures at −40°C to −69°C [*Diao et al.*, 2014; *Jensen et al.*, 2001]. However, the representations of the coexistence between ISS and ice crystals can be oversimplified in general circulation models (GCMs). For example, ISS would be immediately relaxed to ice saturation once ice nucleation occurs in the scheme of *Tompkins et al.* [2007], and other improved process-oriented cirrus schemes still assume homogeneous vapor distribution for in-cloud conditions [*Kärcher and Burkhardt*, 2008; *Wang and Penner*, 2010; *Wang et al.*, 2014]. Thus, the representations of ISS in both clear-sky and in-cloud conditions in GCMs still warrant improvements, and quantifying the potential biases associated with the radiative forcing of ISS would benefit future development of ISS parameterizations.

The radiative forcing of ISS is influenced by its spatial extent (in the vertical and horizontal) as well as the microphysical properties of ice crystals embedded in it. For the spatial scales of ISS, previously, in situ observations from the European Measurement of Ozone and Water Vapor by Airbus In-service Aircraft program have been used to provide a distribution law of the ISS horizontal spatial extent [*Gierens and Spichtinger*, 2000], and radiosonde observations over Lindenberg have been used to derive the vertical depth distribution of ISS layers [*Spichtinger et al.*, 2003]. However, as the recent analyses based on 1 Hz (~200 m horizontal resolution) aircraft-based observations reported, the horizontal scale of ISS has mean and median lengths at ~3 km and 1 km, respectively [*Diao et al.*, 2014]. These results revealed a much patchier spatial structure of ISS conditions than the previously reported ones with an ~150 km median length [*Gierens and Spichtinger*, 2000]. The influences of these microscale ISS, which are on the subgrid scales of most climate model simulations (~10–100 km), have yet to be quantified.

Satellite measurements have been used to estimate the occurrence frequencies of ISS in different seasons, geographical locations, and pressure levels [*Gierens et al.*, 2000; *Kahn et al.*, 2009; *Lamquin et al.*, 2012]. However, the radiative impacts of ISS have not been assessed using high-accuracy in situ observations on a global scale. Furthermore, the correlation between the horizontal and vertical extents of ISS has not been systematically analyzed. Water vapor and ice crystals in cirrus clouds, although both consisting of H_2O molecules, have vastly different impacts on the radiation energy budget. A previous study based on idealized representation of ISS shows that the radiative effects of a typical midlatitude clear-sky ISS region can be significant [*Fusina et al.*, 2007]. Although the outgoing longwave radiation (OLR) only decreases slightly (up to 0.8 W/m^2) due to the absorption by the excess water vapor (EWV) over saturation, if the EWV were replaced by artificially formed thin cirrus, this could produce up to 3 K/d, 38 W/m^2, and 40 W/m^2 differences in heating rates, OLR, and surface flux, respectively. *Tompkins et al.* [2007] and *Gettelman and Kinnison* [2007] examined the potential global impacts of ISS based on simple schemes in the general circulation model. Their sensitivity tests showed that allowing ISS in the simulation leads to decreases in high cloud coverage and increases in water vapor, which change the globally averaged top of the atmosphere (TOA) radiation flux by ~0.8 W/m^2 (0.2 W/m^2 in *Tompkins et al.* [2007]).

In this paper, we quantify the spatial characteristics and radiative impacts of ISS in the UTLS region based on ~200 m horizontal resolution, in situ data obtained from several recent aircraft campaigns. Five National Science Foundation (NSF) flight campaigns on board the NSF/National Center for Atmospheric Research (NCAR) Gulfstream-V (GV) research aircraft are used in this study. In section 2, we will first describe and summarize the primary features of the ISS conditions used in this study. Then we will explain how the radiative effect of ISS is assessed and discuss the results in section 3. We will summarize this study and discuss its significance, as well as caveats, in section 4.

2. ISS Data

2.1. ISS Measurements

In this study, we use the aircraft-based, in situ observations from the NSF GV research aircraft during five campaigns: the Stratosphere Troposphere Analyses of Regional Transport 2008 (START08) campaign [*Pan et al.*, 2010], the High-performance Instrumented Airborne Platform for Environmental Research Pole-to-Pole Observations (HIPPO) from 2009 to 2011 [*Wofsy et al.*, 2011], the Pre-Depression Investigation of Cloud-systems in the Tropics (PREDICT) in 2010 [*Montgomery et al.*, 2012], the Tropical Ocean Troposphere Exchange of Reactive halogen species and Oxygenated VOC (TORERO) in 2012 [*Volkamer et al.*, 2015], and the Deep Convective Clouds and Chemistry Project (DC3) in 2012 [*Barth et al.*, 2015]. All the samples used here are restricted to temperatures ≤ -40°C to eliminate the coexistence of supercooled liquid water droplets with ice crystals.

The 1 Hz relative humidity values are derived from water vapor and temperature measurements during the in situ observations, which have accuracy (and precision) of ~ ±6% (±1%) and ~ ±0.5 K–1 K (±0.01 K), respectively. Water vapor measurements were collected by the Vertical Cavity Surface Emitting Laser (VCSEL) hygrometer [*Zondlo et al.*, 2010], and temperature was recorded by a Rosemount temperature probe. These two measurements contribute to combined uncertainties of ~8%–18% in RHi for temperatures at 233–196 K. The horizontal resolution of the in situ data was ~240 m given the measurement frequency of 1 Hz and mean true air speed of the research aircraft of 240 m/s.

Ice particle measurements in all five campaigns were sampled by the NCAR Fast Two-Dimensional Cloud Probe (Fast-2 DC) [*Stith et al.*, 2014]. For START08 campaign, we combine the additional ice crystal measurements from a second ice probe—the Small Ice Detector-2H instrument (SID-2H)—with the measurements from Fast-2 DC probe for analysis of in-cloud conditions and ice water content. Similar to the in-cloud and clear-sky analyses in a previous study of *Diao et al.* [2015], the in-cloud condition is defined as where at least one ice particle per 16 cm^3 has been detected at 1 Hz scale, while the remaining samples are considered to be clear sky (i.e., cloud-free). The measurement ranges of SID-2H and Fast-2 DC are 5–50 μm and 75–1600 μm, respectively. To alleviate the potential shattering effects of the Fast-2 DC probe, this study analyzes ice water content rather than ice crystal number concentration. Details of the water vapor, temperature, and ice crystal measurements are discussed in *Diao et al.* [2015].

2.2. ISS Characteristics

Based on the aircraft observations, there are 2988 clear-sky ISS samples and 890 in-cloud samples in five campaigns. One ISS sample corresponds to the region where ISS is continuously observed. The length of ISS ranges over several orders of magnitude in scale, from ~100 m to 100 km. In order to better represent the average radiative impact and the properties of ISS, we use the length-weighted average value of total samples in the following presentation (if not otherwise stated):

$$\overline{x} = \Sigma x_i l_i / \Sigma l_i, \tag{1}$$

l_i is the length of each ISS sample and x represents a certain property of ISS (e.g., RH and pressure).

Typically, the research aircraft either conduct vertical profiles or maintain the horizontal flight. In the former case, the aircraft transects through an ISS layer in one direction and likely captures the full depth of the ISS layers. In the latter case, the aircraft maintains horizontal flight with small variations in altitude and pressure and therefore may not capture the real depth of the ISS layers. To remedy the potential incomplete transect in the latter case, we derive a linear correlation between ISS horizontal and vertical extent for each campaign only using samples in the former case: thickness = $a + b$ * length (see Figure S2 in the supporting information). Here a and b are the regression coefficients with $a = 1.2$, -4.0, -5.2, -10.3, and 5.7, $b = 0.003$, 0.024, 0.017, 0.037, and 0.02 for PREDICT, TORERO, DC3, START08, and HIPPO, respectively. The upper limits of the thicknesses of ISS samples used for linear regressions in the five campaigns are 1536, 919, 1689, 1519, and 1799 m, respectively, which denote the maximum thicknesses of the samples used in the regressions. Then we predict the vertical depths of ISS samples in the latter case from their horizontal extents by using the linear regression equations determined above. When a negative thickness is predicted, we use the original measurements for the thickness. When the predicted thickness exceeds the upper limits as denoted above, we set the thickness to be the respective upper limit in each campaign.

From Figure 1, most of the ISS samples are located in the upper troposphere. More than half are less than 100 m thick. Over the tropics, samples in the PREDICT campaign have lower average thickness, lower EWV content, and higher preexisting ice water path (IWP) compared to TORERO. And over the North American continent, the DC3 samples are on average of lower thickness, lower EWV, and higher IWP than the START08 samples. Overall, the length-weighted altitude, RHi, thickness, EWV content, and IWP in all the samples in the five campaigns are 223 hPa, 110.4%, 665 m, 3.0 g/m^2, and 42.3 g/m^2, respectively. See Figure S3 for more discussion on the ISS characteristics.

3. Radiative Effects of ISS in Five Campaigns

3.1. Configurations of the Radiative Transfer Calculation

In order to determine the radiative impacts of ISS, we calculate and compare the radiative quantities under three scenarios: (1) ISS as in situ observed; (2) excluding ISS, by removing the EWV over saturation; and (3) the artificially formed cirrus clouds, by replacing the EWV with artificially formed ice crystals at saturation of the same amount of total water content. The first type of radiative effect of ISS is defined as the difference between Scenarios 2 and 1, which represents the error of neglecting ISS (i.e., excluding the EWV). The second type of radiative effect of ISS is defined as the difference between Scenarios 3 and 1, which represents the error of mistaking the EWV as artificially formed ice crystals. Following *Fusina et al.* [2007], we measure the ISS radiative effects on heating rates (RE_{htr}) by summing up the increases in the lower boundary heating and in the upper boundary cooling:

$$RE_{htr} = |htr(x) - htr(y)|_{upper} + |htr(x) - htr(y)|_{lower}, \tag{2}$$

where x and y denote different scenarios (1–3).

Here we use the rapid radiative transfer model (RRTMG) [*Iacono et al.*, 2008] for calculating the radiative fluxes and heating rates. RRTMG adopts the correlated-k approach and absorption coefficient data determined from line-by-line radiative transfer calculation [*Clough et al.*, 1992]. There are 16 bands in the longwave (10–3250 cm^{-1}) and 14 bands in the shortwave (820–50,000 cm^{-1}), respectively. Modeled sources of extinction include H_2O; O_3; well-mixed greenhouse gases such as CO_2, CH_4, and N_2O; aerosols; clouds; and Rayleigh

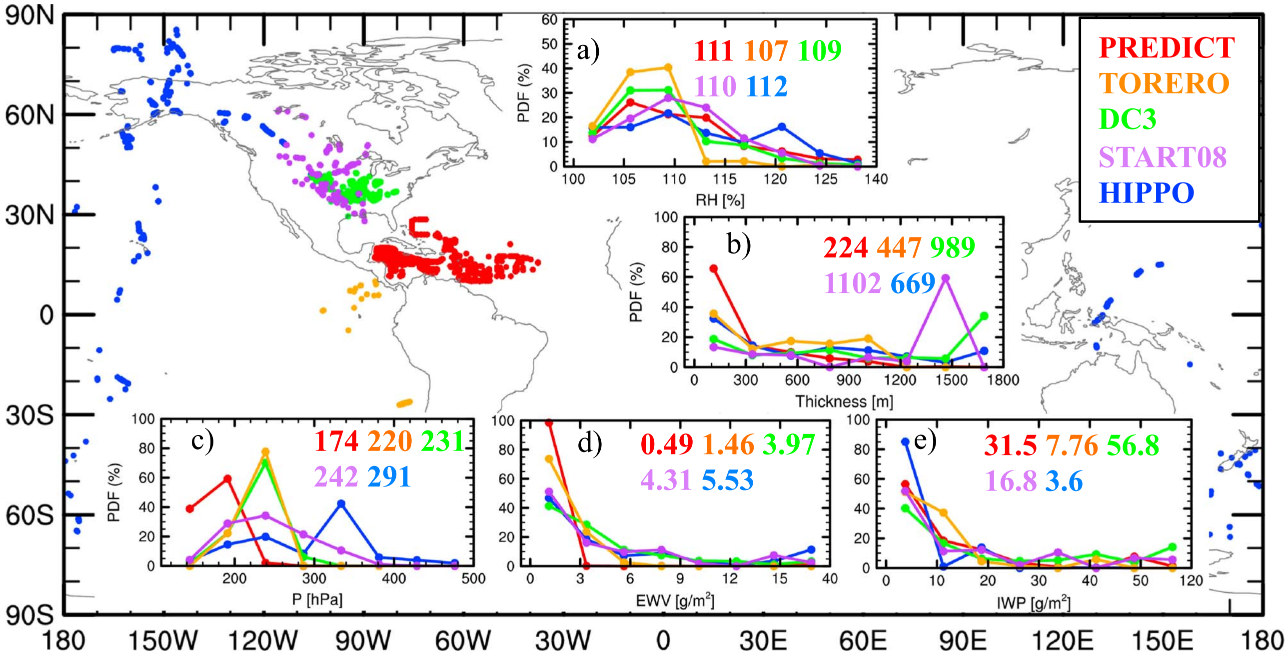

Figure 1. Geographic distributions of the ISS samples. The imbedded plots show the length-weighted probability density functions (in %) of (a) RHi (%), (b) thickness (m), (c) pressure (hPa), (d) excess water vapor content (EWV, g/m^2), and (e) the preexisting ice water path (IWP, g/m^2) in cloudy condition of the ISS samples in each campaign. Numerical values in the figure legends show the length-weighted average values of each ISS characteristic for five flight campaigns.

scattering (shortwave only). The concentrations of well-mixed greenhouse gases are fixed to be the global mean values of year 2010: CO_2: 388 ppm, CH_4: 1.8 ppm, and N_2O: 323 ppb. For cloudy cases, RRTMG uses Monte Carlo Independent Column Approximation [*Pincus et al.*, 2003] to represent subgrid cloud variability. The maximum-random cloud overlapping scheme is used in our calculations. The ERA-Interim atmospheric variables used here include air temperature, specific humidity, ozone mixing ratio, surface pressure, surface temperature, and albedo. For each in situ observed ISS sample, we select the nearest time and location from reanalysis data to gain the input profile for RRTMG calculations. We also set the solar zenith angle appropriate to sample measurement time and location. The top of the profile is set as 1 hPa to be consistent with the reanalysis data. The atmospheric variables are interpolated to 20 hPa thick layers between 1000 hPa and 100 hPa, in addition to 30 layers over 100 hPa.

The radiative effect of ISS is calculated for single ISS layers, which means that only one observed ISS layer, with cloud ice particles as measured, is inserted into each reanalysis profiles and no other cloud layers are considered. Because 63% of the ISS samples are less than 100 m thick (see Figure 1), we calculate the appropriate amount of the EWV in terms of water vapor volume mixing ratio within ISS layers in each 20 hPa layer as

$$q_v = ((d_{\mathrm{rt}} - d_{\mathrm{obs}}) * q_{\mathrm{era}} + d_{\mathrm{obs}} * q_{\mathrm{obs}})/d_{\mathrm{rt}}, \tag{3}$$

where d_{rt} and d_{obs} are the thickness of the model layer (20 hPa) and of the observed ISS sample, respectively. The q_{era} and q_{obs} are the water vapor mixing ratio in ERA-Interim and aircraft observation in the corresponding layer, respectively. The saturation vapor pressure over ice is determined following *Murphy and Koop* [2005]. To avoid spurious dependency of calculated heating rates on the thickness of the model vertical layer (which results from finite differencing in the radiation codes), the radiative effect on heating rates in equation (2) is scaled by the ratio of d_{rt} and d_{obs}:

$$\mathrm{RE}_{\mathrm{htr}} = \left(\left|\mathrm{htr}(x) - \mathrm{htr}(y)\right|_{\mathrm{upper}} + \left|\mathrm{htr}(x) - \mathrm{htr}(y)\right|_{\mathrm{lower}}\right) * \frac{d_{\mathrm{rt}}}{d_{\mathrm{obs}}}. \tag{4}$$

We compared different vertical resolutions (i.e., 5, 10, and 25 hPa) in RRTMG calculations, and the differences are negligible.

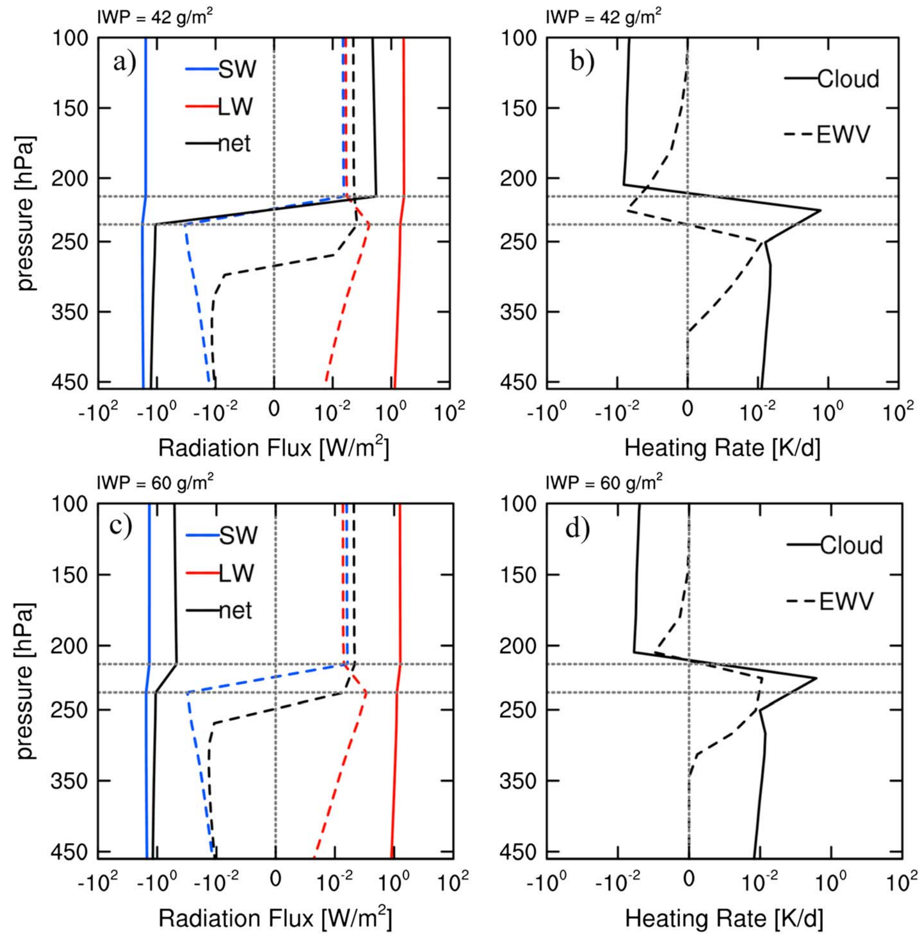

Figure 2. Radiative impacts of ISS with multicampaign average properties (RHi, thickness, pressure, and EWV) on (left column) longwave, shortwave, net radiation flux, and (right column) heating rates. (a and b) With multicampaign average IWP of 42 g/m^2; (c and d) with IWP of 60 g/m^2. The dashed and solid lines denote the radiative effects of removing the excess water vapor (labeled as EWV) and replacing the EWV with cirrus clouds (labelled as cloud), respectively. The horizontal dotted lines denote the vertical boundaries of the ISS layer.

To specify the effective radius (R_{eff}) of artificially formed ice crystals, we use the parameterization given by *Lohmann and Roeckner* [1996]:

$$R_{\text{eff}} = R_0 * (\text{IWC}/\text{IWC}_0)^b, \text{ where } R_0 = 83.8 \ \mu\text{m}, \ b = 0.216, \text{ and } \text{IWC}_0 = 1\text{g/m}^3. \tag{5}$$

We examined the uncertainty in our radiation calculation due to the uncertainty in R_{eff}, by comparing the results obtained using equation (5) to (1) the results obtained when perturbing R_{eff} in equation (5) by 10% while holding the total ice water content unchanged and (2) the results obtained from two different R_{eff} parameterizations based on temperature [*Ou and Liou*, 1995] and ice water content at different latitudes [*Liou et al.*, 2008]. We found that the differences in the radiative effects calculated are generally within 10% under cloudy condition but can be up to 17% for TOA fluxes, 27% for surface fluxes, and 22% for heating rates under clear-sky condition (see Figure S4).

3.2. Two Types of Radiative Effects of ISS

We illustrate in Figure 2 the radiative effects of ISS under the two circumstances described above by using ISS with multicampaign average properties (RHi, thickness, pressure, and EWV) described in section 2.2 and summarize the results averaged from all samples in Table 1.

As shown in Figure 2, the EWV in the ISS layer traps outgoing longwave radiation and thus increases the net downward flux at TOA. The EWV also slightly decreases the shortwave (and thus the net) downward radiation

Table 1. Radiative Effects of ISS on the TOA and Surface Net Radiation Fluxes (Units: W/m^2) and on Heating Rates (HTR, Units: K/d)[a]

Campaign	f_{clear}/ f_{cloudy}	Neglecting EWV (Clear-Sky/In-cloud/Average)						Replacing EWV With Cirrus Cloud (Clear-Sky/In-cloud/Average)								
		TOA			HTR			TOA			surface			HTR		
PREDICT	0.15/0.64	−0.02	−0.02	−0.02	0.14	0.06	0.06	1.33	0.57	0.56	−1.54	−0.58	−0.60	3.11	0.96	1.08
TORERO	0.27/0.47	−0.04	−0.04	−0.03	0.07	0.06	0.05	6.61	3.91	3.62	−2.44	−2.02	−1.61	3.56	1.91	1.86
DC3	0.10/0.72	−0.04	−0.07	−0.05	0.12	0.06	0.06	4.66	2.65	2.37	−2.24	−3.53	−2.77	3.53	1.49	1.43
START08	0.30/0.55	−0.09	−0.09	−0.08	0.07	0.05	005	11.55	6.77	7.19	−5.21	−6.59	−5.19	2.70	1.94	1.88
HIPPO	0.38/0.52	−0.10	−0.09	−0.09	0.10	0.07	0.07	5.92	3.77	4.21	−6.78	−5.24	−5.30	2.14	1.61	1.65
Multicampaign average	0.22/0.60	−0.05	−0.06	−0.05	0.12	0.06	0.06	4.24	2.60	2.49	−3.65	−3.16	−2.70	2.82	1.41	1.47

[a]f_{clear} ($f_{in\text{-}cloud}$) is the fraction of clear-sky (in-cloud) ISS samples in terms of length.

flux at the surface. There is a warming effect at the bottom of the ISS layer due to enhanced absorption of surface emission by the EWV, while a cooling effect is seen at the top of the layer due to enhanced radiative cooling there. The radiative effects of EWV with different preexisting IWP are similar. Note that the radiative effects of neglecting the EWV are of the opposite signs compared to the results shown in Figure 2. In comparison, when the EWV is replaced by cirrus cloud, the radiative effects are much stronger because of the larger optical depth caused by ice particles compared to water vapor. When the preexisting IWP is large enough, the impact on shortwave radiation will dominate and bring a cooling effect at TOA.

Figures 3a–3c show the radiative effects of removing the EWV in all the clear-sky and in-cloud samples from the five campaigns. In general, when RHi increases, the magnitude of the radiative effect increases. It is noticed that tropical samples in campaign PREDICT have a weaker effect compared to those in TORERO with the same RHi. Over the North America, ISS samples in DC3 have smaller radiative effects than those in START08. The reason lies in that at the same RHi, the samples in PREDICT and DC3 tend to have relatively smaller thickness and less EWV content.

Our calculations show that neglecting the EWV, the net downward radiation at TOA can decrease up to 0.4 W/m^2 in clear-sky conditions (obtained from a sample with a thickness of 1.24 km and RHi of 134%). This result is comparable with that of *Fusina et al.* [2007], who calculated 0.8 W/m^2 effect from a relatively thick ISS layer with 160% RHi and 1.2 km thickness. The average impacts on TOA radiation flux and heating rates are −0.05 W/m^2 and 0.12 K/d in clear-sky conditions. At the surface, the average impact is generally less than 0.01 W/m^2, which is negligible and thus omitted from Table 1. In cloudy condition, the radiative effects of the EWV are similar to those in clear-sky conditions.

In comparison, if the EWV were mistaken as cirrus clouds, the additional ice crystals would generate larger radiative effects compared with water vapor (see Figure S5). The changes in TOA and surface net radiation due to artificially formed clouds replacing the EWV in the clear-sky ISS samples are 54 W/m^2 and −7.7 W/m^2 at maximum and 4.24 W/m^2 and −3.65 W/m^2 on average, respectively. The impacts on heating rates are up to 16 K/d, average to 2.82 K/d through heating the bottom and cooling the top of the ISS layers.

In the in-cloud ISS samples in which ISS coexists with ice clouds, the radiation fluxes at TOA and the surface change by up to 31.1 W/m^2 and −8.64 W/m^2, respectively; the heating rates change up to 13.2 K/d. All the in-cloud ISS samples included, the average radiative impacts are 2.60 W/m^2 at TOA, −3.16 W/m^2 at the surface and 1.41 K/d on heating rates, smaller than those of the clear-sky ISS samples. Interestingly, we find that the radiative effects are dependent on the amount of preexisting ice in the ISS samples (see Figures 3j–3l). Two transition thresholds are found when replacing EWV with artificially formed ice crystals, i.e., the preexisting IWP values of 7 g/m^2 and 53 g/m^2. The radiative effect exhibits a maximum at ~7 g/m^2 IWP, and at TOA it becomes negative as preexisting IWP exceeds 53 g/m^2 (with cloud visible optical depth being ~1.8). As illustrated in Figure 2, the change in sign in the TOA radiative effect (compare the black solid lines in Figures 2a and 2c) is due the fact that to the reflected shortwave radiation becomes larger than the absorption of longwave radiation at higher IWP values. In 50 of the 890 in-cloud samples, artificially formed ice clouds have cooling effects at TOA, with an average magnitude of −1.24 W/m^2. The few samples in HIPPO with lower IWP and negative radiative effects at TOA are likely due to larger solar zenith angle and lower surface temperature. Nevertheless, for the majority of the ISS samples, the impacts of the preexisting IWP are much larger than other factors (see Figure S6).

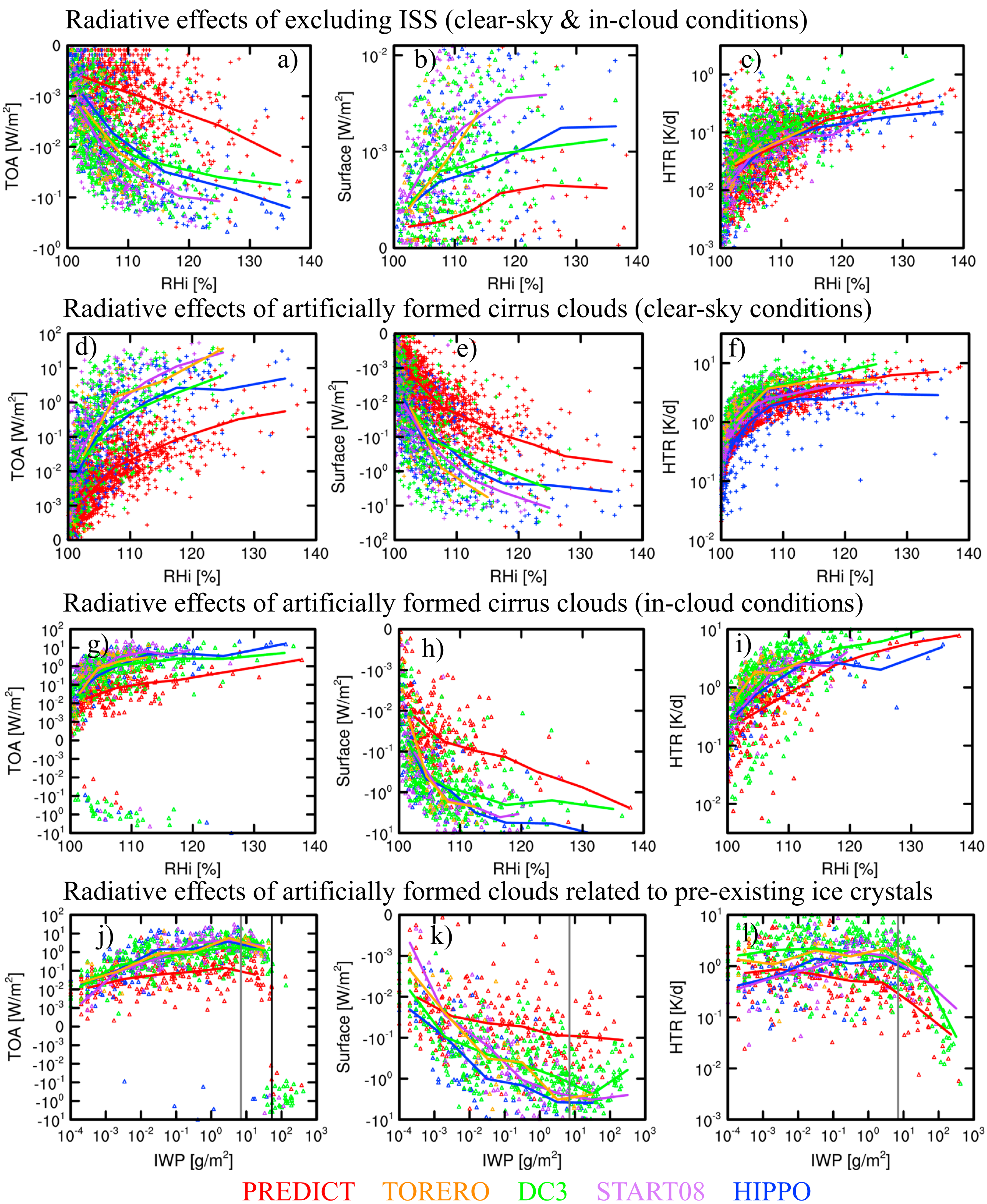

Figure 3. Two types of radiative effects on (left column) TOA net radiation, (middle column) surface net radiation, and (right column) heating rates. (a–c) The radiative effect of excluding the EWV in clear-sky and cloudy condition. (d–i) The radiative effects of artificially formed clouds in clear-sky and cloudy condition. (j–l) The radiative effects binned with respect to the ice water path (IWP) of the preexisting cirrus clouds. The grey and black lines represent IWP values of 7 g/m^2 and 53 g/m^2, respectively, which are the thresholds for transitions in radiative effect of artificially formed clouds. Samples with radiative effect less than 1e-4 W/m^2 (or K/d) are ignored in this figure. See Figure S1 for a simplified version of this figure.

For each type of radiative effect of ISS (EWV is neglected or replaced by cirrus cloud), an average value in all-sky conditions can be obtained by averaging over all the clear-sky, in-cloud ISS, and non-ISS samples. Here we calculate this average radiative effect ($RE_{all - sky}$) as

$$RE_{all\text{-}sky} = f_{clear}{*}RE_{clear} + f_{cloudy}{*}RE_{cloudy} + f_{nonISS}{*}RE_{nonISS}, \quad (6)$$

f_{clear}, f_{cloudy}, and f_{nonISS} are the fractions in length of clear-sky ISS, in-cloud ISS, and non-ISS ice cloud samples with respect to the total length of these three kinds of samples and RE_{clear} and RE_{cloudy} are the length-weighted radiative effects of ISS in clear-sky and in-cloud conditions, respectively. Here RE_{nonISS} equals zero. As shown in Table 1, the average radiative effects of neglecting the EWV are -0.05 W/m^2 on TOA radiation flux, less than 0.01 W/m^2 on surface radiation, and 0.06 K/d on vertical heating rates. The radiative effects of artificially formed cirrus clouds depend on the amount of preexisting ice, and on average these artificially formed clouds lead to a warming effect of 2.49 W/m^2 at TOA, a cooling effect of -2.7 W/m^2 at the surface, and a perturbation of 1.47 K/d in heating rates.

4. Conclusions and Discussions

In this study, the properties of ISS are investigated based on the in situ observed ISS data obtained from five campaigns over North America, the Caribbean Sea, and the Central and Eastern Pacific Ocean. Using the RRTMG model, we quantified the potential biases in radiation fluxes and heating rates when the observed ISS is replaced by saturation conditions or artificially formed cirrus clouds.

Replacing EWV with cirrus clouds leads to more than 1 order of magnitude higher increases than simply neglecting EWV. The effects of the artificially formed clouds on the TOA net radiation range from +0.56 W/m^2 to +7.19 W/m^2, in addition to an average surface cooling effect of -2.7 W/m^2 and a 1.47 K/d change on heating rates.

We find that although the radiative effects of ISS (both removing and replacing EWV) generally increase with RHi, there is dependence on background IWP. For instance, when replacing the EWV by ice crystals, the effects on TOA radiation change from a warming effect to a cooling effect as the preexisting IWP becomes greater than about 53 g/m^2, which corresponds to a visible optical depth of ~1.8. We note that the observations used in this study sampled both in situ and convectively formed cirrus clouds. Quantifications of the radiative effects of ISS associated with different cloud origins, which can be determined using trajectory-based method [e.g., *Wernli et al.*, 2016], are suggested for future work.

Our results suggest that in numerical models, the parameterization of RHi thresholds of ice nucleation can have large potential impacts on the net radiation at the TOA and surface, as well as in the vertical heating rate profile. For example, had all the ISS that exists above certain ice nucleation thresholds been arbitrarily converted into ice crystals, large biases would potentially be generated in the local radiative forcing. In addition, our results show that the coexistence of ISS and ice crystals is important for correctly representing the magnitude and signs of radiative forcing. As a previous observational analysis reported, the coexistence of ISS and ice crystals contributes to ~10% of the lifetime during the evolution of cirrus clouds [*Diao et al.*, 2013]. Whether such coexistence between ISS and ice crystals can be represented correctly in model simulations has yet to be validated. The results from this work help to estimate the potential improvements in radiative forcing that can be achieved if constraining the model simulations with in situ observations at various geographical locations.

Acknowledgments
We acknowledge the ECMWF for the ERA-Interim data (http://apps.ecmwf.int/datasets/data/interim-full-moda/), the NSF for the observed ISS data, and the Atmospheric Environment Research for RRTMG model (http://rtweb.aer.com/rrtm_frame.html) used in this study. X.T. is supported by a visiting student fellowship of China Scholarship Council. Y. Huang acknowledges the grants support from the Natural Sciences and Engineering Research Council of Canada (RGPIN 418305-13) and the Fonds de recherche du Quebec–Nature et technologies (PR-190145). M.D. acknowledges the support of National Center for Atmospheric Research Advanced Study Program for her postdoctoral research in 2013–2015. Y. Hu acknowledges the grants from the National Natural Science Foundation of China (41375072 and 41530423). NCAR is sponsored by the National Science Foundation. For the observation analysis on five NSF campaigns (HIPPO Global, START08, PREDICT, DC3, and TORERO), we thank the efforts of flight, technical, and mechanical crews at the NCAR/Earth Observing Laboratory. M.A. Zondlo, M. Diao, J. DiGangi, and S.P. Beaton provided the field support and laboratory calibration of the VCSEL hygrometer. A. Bansemer, A.J. Heymsfield, D.C. Rogers, and C.J. Webster provided support on the SID-2H instrument and Fast-2 DC probes. We acknowledge the observations from the European Union INCA campaign, with recent data updates from Ulrich Schumann and Andreas Minikin. All data used in this study are free and publicly available. The aircraft observations for individual NSF campaigns were obtained at http://data.eol.ucar.edu/codiac/

References

Barth, M. C., et al. (2015), The deep convective clouds and chemistry (DC3) field campaign, *Bull. Am. Meteorol. Soc.*, *96*(8), 1281–1310, doi:10.1175/BAMS-D-13-00290.1.

Brewer, A. W. (1946), Condensation trails, *Weather*, *1*, 34–40.

Clough, S. A., M. J. Iacono, and J. Moncet (1992), Line-by-line calculations of atmospheric fluxes and cooling rates: Application to water vapor, *J. Geophys. Res.*, *97*, 15,761–15,785, doi:10.1029/92JD01419.

Comstock, J. M., T. P. Ackerman, and D. D. Turner (2004), Evidence of high ice supersaturation in cirrus clouds using ARM Raman lidar measurements, *Geophys. Res. Lett.*, *31*, L11106, doi:10.1029/2004GL019705.

Diao, M., M. A. Zondlo, A. J. Heymsfield, S. P. Beaton, and D. C. Rogers (2013), Evolution of ice crystal regions on the microscale based on in situ observations, *Geophys. Res. Lett.*, *40*, 3473–3478, doi:10.1002/grl.50665.

Diao, M., M. A. Zondlo, A. J. Heymsfield, L. M. Avallone, M. E. Paige, S. P. Beaton, T. Campos, and D. C. Rogers (2014), Cloud-scale ice supersaturated regions spatially correlate with high water vapor heterogeneities, *Atmos. Chem. Phys.*, *14*, 2639–2656, doi:10.5194/acp-14-2639-2014.

Diao, M., J. B. Jensen, L. L. Pan, C. R. Homeyer, S. Honomichl, J. F. Bresch, and A. Bansemer (2015), Distributions of ice supersaturation and ice crystals from airborne observations in relation to upper tropospheric dynamical boundaries, *J. Geophys. Res. Atmos.*, *120*, 5101–5121, doi:10.1002/2015JD023139.

Fusina, F., P. Spichtinger, and U. Lohmann (2007), Impact of ice supersaturated regions and thin cirrus on radiation in the midlatitudes, *J. Geophys. Res.*, *112*, D24S14, doi:10.1029/2007JD008449.

Gayet, J. F., J. Ovarlez, V. Shcherbakov, J. Ström, U. Schumann, A. Minikin, F. Auriol, A. Petzold, and M. Monier (2004), Cirrus cloud microphysical and optical properties at southern and northern midlatitudes during the INCA experiment, *J. Geophys. Res.*, *109*, D20206, doi:10.1029/2004JD004803.

Gettelman, A., and D. E. Kinnison (2007), The global impact of supersaturation in a coupled chemistry-climate model, *Atmos. Chem. Phys.*, *7*, 1629–1643, doi:10.5194/acp-7-1629-2007.

Gettelman, A., E. J. Fetzer, A. Eldering, and F. W. Irion (2006), The global distribution of supersaturation in the upper troposphere from the Atmospheric Infrared Sounder, *J. Clim.*, *19*(23), 6089–6103, doi:10.1175/JCLI3955.1.

Gierens, K., and P. Spichtinger (2000), On the size distribution of ice-supersaturated regions in the upper troposphere and lowermost stratosphere, *Ann. Geophys.*, *18*(4), 499–504, doi:10.1007/s00585-000-0499-7.

Gierens, K., U. Schumann, M. Helten, H. Smit, and A. Marenco (1999), A distribution law for relative humidity in the upper troposphere and lower stratosphere derived from three years of MOZAIC measurements, *Ann. Geophys.*, *17*(9), 1218–1226, doi:10.1007/s00585-999-1218-7.

Gierens, K., U. Schumann, M. Helten, H. Smit, and P.-H. Wang (2000), Ice-supersaturated regions and subvisible cirrus in the northern midlatitude upper troposphere, *J. Geophys. Res.*, *105*, 22,743–22,753, doi:10.1029/2000JD900341.

Heymsfield, A. J., L. M. Miloshevich, C. H. Twohy, G. Sachse, and S. Oltmans (1998), Upper-tropospheric relative humidity observations and implications for cirrus ice nucleation, *Geophys. Res. Lett.*, *25*(9), 1343, doi:10.1029/98GL01089.

Iacono, M. J., J. S. Delamere, E. J. Mlawer, M. W. Shephard, S. A. Clough, and W. D. Collins (2008), Radiative forcing by long-lived greenhouse gases: Calculations with the AER radiative transfer models, *J. Geophys. Res.*, *113*, D13103, doi:10.1029/2008JD009944.

Jensen, E. J., O. B. Toon, S. A. Vay, J. Ovarlez, R. May, T. P. Bui, C. H. Twohy, B. W. Gandrud, R. F. Pueschel, and U. Schumann (2001), Prevalence of ice-supersaturated regions in the upper troposphere: Implications for optically thin ice cloud formation, *J. Geophys. Res.*, *106*, 17,253–17,266, doi:10.1029/2000JD900526.

Jensen, E. J., G. Diskin, R. P. Lawson, S. Lance, T. P. Bui, D. Hlavka, M. McGill, L. Pfister, O. B. Toon, and R. Gao (2013), Ice nucleation and dehydration in the tropical tropopause layer, *Proc. Natl. Acad. Sci. U.S.A.*, *110*, 2041–2046, doi:10.1073/pnas.1217104110.

Kahn, B. H., A. Gettelman, E. J. Fetzer, A. Eldering, and C. K. Liang (2009), Cloudy and clear-sky relative humidity in the upper troposphere observed by the A-train, *J. Geophys. Res.*, *114*, D00H02, doi:10.1029/2009JD011738.

Kärcher, B., and U. Burkhardt (2008), A cirrus cloud scheme for general circulation models, *Q. J. R. Meteorol. Soc.*, *134*(635), 1439–1461, doi:10.1002/qj.301.

Krämer, M., et al. (2008), Ice supersaturations and cirrus cloud crystal numbers, *Atmos. Chem. Phys. Discuss.*, *8*(6), 21,089–21,128, doi:10.5194/acpd-8-21089-2008.

Lamquin, N., C. J. Stubenrauch, K. Gierens, U. Burkhardt, and H. Smit (2012), A global climatology of upper-tropospheric ice supersaturation occurrence inferred from the Atmospheric Infrared Sounder calibrated by MOZAIC, *Atmos. Chem. Phys.*, *12*(1), 381–405, doi:10.5194/acp-12-381-2012.

Liou, K. N., Y. Gu, Q. Yue, and G. McFarguhar (2008), On the correlation between ice water content and ice crystal size and its application to radiative transfer and general circulation models, *Geophys. Res. Lett.*, *35*, L13805, doi:10.1029/2008GL033918.

Lohmann, U., and E. Roeckner (1996), Design and performance of a new cloud microphysics scheme developed for the ECHAM general circulation model, *Clim. Dyn.*, *12*(8), 557–572, doi:10.1007/BF00207939.

Meerkötter, R., U. Schumann, D. R. Doelling, P. Minnis, T. Nakajima, Y. Tsushima, and R. Meerkotter (1999), Radiative forcing by contrails, *Ann. Geophys.*, *17*(8), 1080–1094, doi:10.1007/s00585-999-1080-7.

Montgomery, M., et al. (2012), The Pre-Depression Investigation of Cloud systems in the Tropics (PREDICT) experiment: Scientific basis, new analysis tools and some first results, *Bull. Am. Meteorol. Soc.*, *93*, 153–172.

Murphy, D. M., and T. Koop (2005), Review of the vapour pressures of ice and supercooled water for atmospheric applications, *Q. J. R. Meteorol. Soc.*, *131*(608), 1539–1565, doi:10.1256/qj.04.94.

Ou, S., and K. N. Liou (1995), Ice microphysics and climatic temperature feedback, *Atmos. Res.*, *35*(2–4), 127–138, doi:10.1016/0169-8095(94)00014-5.

Pan, L. L., et al. (2010), The Stratosphere–Troposphere Analyses of Regional Transport 2008 Experiment, *Bull. Am. Meteorol. Soc.*, *91*(3), 327–342, doi:10.1175/2009BAMS2865.1.

Pincus, R., H. W. Barker, and J.-J. Morcrette (2003), A fast, flexible, approximate technique for computing radiative transfer in inhomogeneous cloud fields, *J. Geophys. Res.*, *108*(D13), 4376, doi:10.1029/2002JD003322.

Schumann, U., B. Mayer, K. Graf, and H. Mannstein (2012), A parametric radiative forcing model for contrail cirrus, *J. Appl. Meteorol. Climatol.*, *51*(7), 1391–1406, doi:10.1175/JAMC-D-11-0242.1.

Spichtinger, P., K. Gierens, U. Leiterer, and H. Dier (2003), Ice supersaturation in the tropopause region over Lindenberg, Germany, *Meteorol. Z.*, *12*(3), 143–156, doi:10.1127/0941-2948/2003/0012-0143.

Stith, J. L., L. M. Avallone, A. Bansemer, B. Basarab, S. W. Dorsi, B. Fuchs, R. P. Lawson, D. C. Rogers, S. Rutledge, and D. W. Toohey (2014), Ice particles in the upper anvil regions of midlatitude continental thunderstorms: The case for frozen-drop aggregates, *Atmos. Chem. Phys.*, *14*(4), 1973–1985.

Tompkins, A. M., K. Gierens, and G. Rädel (2007), Ice supersaturation in the ECMWF integrated forecast system, *Q. J. R. Meteorol. Soc.*, *133*(622), 53–63, doi:10.1002/qj.14.

Volkamer, R., et al. (2015), Aircraft measurements of BrO, IO, glyoxal, NO2, H2O, O2–O2 and aerosol extinction profiles in the tropics: Comparison with aircraft-/ship-based in situ and lidar measurements, *Atmos. Meas. Tech.*, *8*(5), 2121–2148, doi:10.5194/amt-8-2121-2015.

Wang, M., and J. E. Penner (2010), Cirrus clouds in a global climate model with a statistical cirrus cloud scheme, *Atmos. Chem. Phys.*, *10*(12), 5449–5474, doi:10.5194/acp-10-5449-2010.

Wang, M., X. Liu, K. Zhang, and J. M. Comstock (2014), Aerosol effects on cirrus through ice nucleation in the Community Atmosphere Model CAM5 with a statistical cirrus scheme, *J. Adv. Model. Earth Syst.*, *6*(3), 756–776, doi:10.1002/2014MS000339.

Wernli, H., M. Boettcher, H. Joos, A. K. Miltenberger, and P. Spichtinger (2016), A trajectory-based classification of ERA-Interim ice clouds in the region of the North Atlantic storm track, *Geophys. Res. Lett.*, *43*, 6657–6664, doi:10.1002/2016GL068922.

Wofsy, S. C., et al. (2011), HIAPER Pole-to-Pole Observations (HIPPO): Fine-grained, global-scale measurements of climatically important atmospheric gases and aerosols, *Philos. Trans. R. Soc. B*, *369*(1943), 2073–2086, doi:10.1098/rsta.2010.0313.

Zondlo, M. A., M. E. Paige, S. M. Massick, and J. A. Silver (2010), Vertical cavity laser hygrometer for the National Science Foundation Gulfstream-V aircraft, *J. Geophys. Res.*, *115*, D20309, doi:10.1029/2010JD014445.